Multiple mobile excitons manifested as sidebands in metallic phase of $TaSe_3$

J.-Z. Ma[1,2*], S.-M. Nie[3], X. Gui[4], M. Naamneh[1], J. Jandke[1], C. Y. Xi[5], J. L. Zhang[5], T. Shang[6], Y.M. Xiong[5], I. Kapon[7], N. Kumar[8], Y. A. Soh[8], D. Gosalbezmartinez[9], O. Yazyev[9], W.H. Fan[10,11], H. Hübener[12], U. D. Giovannini[12], N. Plumb[1], M. Radovic[1], M. A. Sentef[12], W.-W. Xie[13], Z. Wang[10,11], C. Mudry[14], M. Muller[14*], M. Shi[1*].

[1] *Swiss Light Source, Paul Scherrer Institute, CH-5232 Villigen PSI, Switzerland*

[2] *Department of Physics, City University of Hong Kong, Kowloon, Hong Kong*

[3] *Department of Materials Science and Engineering, Stanford University, Stanford, CA 94305, United States*

[4] *Department of Chemistry, Princeton University, Princeton, New Jersey 08540, USA*

[5] *Anhui Province Key Laboratory of Condensed Matter Physics at Extreme Conditions, High Magnetic Field Laboratory, Chinese Academy of Sciences, Hefei, Anhui 230031, China*

[6] *Laboratory for Multiscale Materials Experiments, Paul Scherrer Institute, CH-5232 Villigen PSI, Switzerland*

[7] *Department of Quantum Matter Physics, University of Geneva, 24 Quai Ernest-Ansermet, 1211 Geneva, Switzerland*

[8] *Paul Scherrer Institute, CH-5232 Villigen PSI, Switzerland*

[9] *Institute of Physics, Ecole Polytechnique Fédérale de Lausanne (EPFL), CH-1015 Lausanne, Switzerland*

[10] *Beijing National Laboratory for Condensed Matter Physics and Institute of Physics, Chinese Academy of Sciences, Beijing 100190, China*

[11] *University of Chinese Academy of Sciences, Beijing 100049, China*

[12] *Max Planck Institute for the Structure and Dynamics of Matter and Center for Free Electron Laser Science, 22761 Hamburg, Germany*

[13] *Department of Chemistry and Chemical Biology, Rutgers University, Piscataway, New Jersey 08854, USA*

[14] *Condensed Matter Theory Group, Paul Scherrer Institute, CH-5232 Villigen PSI, Switzerland*

**Corresponding to: junzhang.ma@psi.ch, markus.mueller@psi.ch, ming.shi@psi.ch*

Excitons are bound states between electrons and holes, whose charge neutrality and a priori itinerant nature make them interesting as potential transmitters of information. However, the demonstration of the mobility of such composite excitations has remained inaccessible to traditional optical experiments which only create and detect excitons with negligible momentum or group velocity. Here, we use angle-resolved photoemission spectroscopy (ARPES) to detect dispersing excitons in the quasi-one-dimensional metallic trichalcogenide $TaSe_3$. While screening usually suppresses exciton formation in metals, the low density of conduction electrons, the low dimensionality, and two many-body effects in $TaSe_3$ favor them. First, the conduction band is renormalized close to the Fermi surface, forming a band of heavy polarons. Second, the poorly screened interaction between a photo-induced valence hole and these polarons leads to various distinct excitonic bound states, which we interpret as intrachain and interchain excitons, and possibly even trions. The thresholds for the formation of a photohole together with an exciton show up in the form of unusual side bands in the ARPES spectra. They are nearly parallel to the bare valence band, but lie at lower excitation energies. Furthermore, we find that the energy separation of the side bands can be tuned by surface doping.

Introduction. Low-dimensional electronic systems with a low density of charge carriers n_c exhibit interesting many-body effects. Indeed, their Fermi energy is low compared to the strength of typical Coulomb interactions, which are poorly screened due to the low n_c. Moreover, interaction effects are enhanced by the low dimensionality. They manifest themselves in the formation of non-Fermi liquid gapless ground states such as metallic Luttinger liquids or gapped ground states such as insulating Wigner crystals and other kinds of charge density waves[1,2]. Not only the ground state of such strongly interacting systems, but also their excitations exhibit interesting strong coupling phenomena. In particular, the attraction between negatively charged electrons and positively charged holes can lead to bound states in the excitation spectrum, usually referred to as excitons[3–8], and this tendency

is enhanced in low dimensions. While the creation of non-moving (i.e., with electrons and holes locate at the minimum/maximum of conduction/valence bands with zero group velocity) excitons by optical excitation is fairly standard[5,6,8], the observation of mobile bound states with sharp dispersions in *metals* has remained elusive for various reasons (while distinct branches of dispersing excitons have been observed very recently in free-standing monolayer WSe_2, a two-dimensional Dirac band insulator, by momentum-resolved electron energy-loss spectroscopy[9]). Exciting a moving bound state with light only involves a higher-order process due to momentum conservation. In photoemission, one has to create a (moving) valence hole and simultaneously excite a particle-hole pair in the conduction band. Since the cross section of such processes scales with the interaction strength is extremely weak, it is enhanced though in the presence of a small Fermi sea where screening is weak and typical momentum transfers are small, which entails large Coulomb matrix elements. Nevertheless, such multi-particle excitations have a continuous spectrum whose lower edge needs to be sufficiently sharp to be detected by ARPES. For phase space reasons this condition is more likely met in quasi-one-dimensional (Q1D) systems. Low dimensionality also favors the visibility of exciton branches since it enhances the binding energy, and thus induces a clear separation of the threshold for bound state excitations from the continuum of three unbound particles. All these reasons favor Q1D metals with a small Fermi sea for the search of dispersing excitons.

In addition to a low dimensionality and low carrier density, exciton formation in a metal is further enhanced if the involved quasiparticles are fairly heavy, which increases the binding energy of the resulting exciton. The mass of dilute conduction electrons can be substantially increased by their strong coupling to relatively soft bosons (phonons or magnons, say), which results in heavy quasiparticles close to the Fermi energy. These three ingredients seem to be present in the well-known Q1D material $TaSe_3$, which makes this material a prime candidate to detect excitonic effects using ARPES. As we will see, the interplay of dilute conduction electrons, low effective dimensionality, and heavy quasiparticles seems to result not only in a single excitonic branch of excitations, but even in multiple flavors of "sidebands", suggesting the possibility of creating bound states with different internal structure.

Main experimental results. We have studied the metallic phase of $TaSe_3$ using ARPES. We observe the following features at low temperature. (1) Several replica (or side valence) bands appear *exclusively above* a pronounced valence band - in contrast to most ARPES spectra that report side bands; see Supplementary Material. (2) Their dispersions are roughly parallel to each other and to that of the valence band. (3) When the surface carrier density is increased by doping, the energy separations between the side valence bands increase. (4) The conduction band is heavily renormalized, the coherent quasiparticle peak following a W-shaped dispersion. As we will argue, observations (1-4) suggest that the

side valence bands result from strong coupling between the valence and conduction electrons and involve *mobile* bound states (excitons, and perhaps trions) that have not been observed so far using ARPES. Up to now, ARPES has detected excitonic physics only in the form of the consequences of excitonic condensation, as seen e.g. in the electronic structure of Ta_2NiSe_5 near the Fermi level[10], or through the band folding due to a finite momentum condensate, e.g., in 1T $TiSe_2$[11].

Material characterization. The trichalcogenide $TaSe_3$ is a representative of the family of crystals XT_3 where X belongs to either the group IVB (Ti, Zr, Hf) or the group VB (Nb, Ta), and T is a chalcogen from the group VIA (S, Se, Te). The crystal $TaSe_3$ consists of covalently bonded layers, stacked and held together by much weaker van der Waals forces along the direction $(10\bar{1})$[12,13]. Each layer consists of chains oriented along the b-axis, see Figs. 1a-b, with strongly anisotropic electric and optical response resulting in an effective Q1D character of the material. The crystal $TaSe_3$ is so far the only known example from this family that is a metal at high temperature and becomes superconducting below 2K without a charge density wave (CDW) phase transition[14–21].

The crystalline structure of $TaSe_3$ is monoclinic with the space group $P2_1/m$ (SG11) (see Figs. 1a-b). The selenium atoms are located at the vertices of triangular prisms with three faces parallel to the b-axis and a tantalum atom at their centre. These prisms are covalently stacked along the b-axis and form parallel one-dimensional (1D) chains (see Fig. 1b). The unit cell viewed along the b-axis contains four triangular prisms (see Fig. 1a), with covalent bonds along the (101) direction. Thus, the natural cleavage plane is the $(10\bar{1})$ surface. The corresponding bulk Brillouin zone (BBZ) and the $(10\bar{1})$ surface Brillouin zone (SBZ) are shown in Fig. 1c. For the SBZ we choose a coordinate system such that (k_x; k_y) denote the components of momentum along (101) and (010), respectively.

Band structure from ARPES. We have studied systematically the electronic structure of $TaSe_3$ with ARPES on the *in situ* cleaved surface $(10\bar{1})$. The intersection of the small three-dimensional (3D) Fermi surface (FS) with a plane spanned by momenta conjugate to the crystalline directions b and $a + c$ is seen as the region of highest intensity in Fig. 1d. Figure 1e (Γ-Y cut) shows hole-like valence bands with maxima at the zone centre Γ, dispersing from 0.1eV to 2eV. Figure 1f (X-S cut) shows an electron-like conduction band with minimum at the mid-point X on one zone edge of the BBZ. The strong anisotropy in the ac plane results in a FS in the form of an elongated elliptical electron pocket centred at X, see Fig. 1d. The strong dispersion along the b-axis leads to a short minor axis along the X-S direction, while the weaker dispersion perpendicular to the chains results in a long major axis of the pocket along X-Γ. There is no good nesting wave vector for the FS of $TaSe_3$ shown in Fig. 1d. This empirical observation might rationalize why the CDW phase is absent in $TaSe_3$. A cut of the FS by a plane in momentum space defined by fixing $k_x = 0$ is

shown in Fig. 1g, where the photon energy $h\nu$ is used to explore momenta normal to the cleavage plane. The FS is seen to be an elliptical cylinder elongated along the stacking direction, which reflects the weak but finite dispersion in that direction. The similarity of the spectra in Figs. 1h-j, corresponding to different normal momenta, also demonstrates the weak coupling between the stacked layers. However, Fig. 1k shows a definite, if small, dependence on the incoming photon energy, which we take as evidence for these bands being bulk as opposed to surface bands.

Side valence bands. In this paper, we focus our attention on remarkable spectral features that look like replica or side valence bands (SVBs). They can be seen in the energy distribution curves (EDC) of the ARPES spectra, as we now explain. We show in Fig. 2a the band structure of $TaSe_3$ along the X-S direction in the BBZ predicted by density functional theory (DFT), as explained in the Methods section. There is one conduction band coloured in green, lying above five valence bands. The valence band closest to the conduction band is coloured in purple and will be referred to as the main valence band (MVB). The other lower lying valence bands are coloured in blue. These DFT bands match the five bands measured in Fig. 2b. The EDC along the green line with fixed $k_y \approx 0.2$ Å^{-1}in Fig. 2b is shown in the boxed inset. The arrows indicate local maxima of this EDC. Upon varying k_y these local maxima move, defining SVB dispersions. Those are bounded from below by the MVB which is sharper both in width and intensity. The MVB and the SVBs become better visible in the curvature intensity plot of Fig. 2c associated with the data of Fig. 2b, (the colour scale being related to the curvature of the ARPES intensity). For reference, Fig. 2d shows the schematic of band dispersion in Fig. 2c. The dispersions of the MVB and SVBs are approximately symmetric about X. The MVB, identified by a purple arrow, shows the largest intensity. Three SVBs are identified by tilted red arrows. We only observe side bands of the MVB, but none of either the conduction band, or of the deeper and steeper valence bands.

Close to the X point, there is no observable intensity that could be clearly assigned to either SVBs or to the MVB. In Fig. 2d the evolution of the MVB away from large momenta (where its peak is well resolved) is indicated by a dashed segment, delineating the "nose" predicted by DFT. We also indicate the possible continuation of SVBs as they approach the spectral features associated to the conduction band, coloured in green in both Fig. 2c and Fig. 2d. Those are of a polaronic origin, as we now explain. As their specifics are important to understand the exciton formation, we now describe them in more detail.

Polaron band. For a typical representative of the family XT_3, the FS is nested, which induces a CDW instability, as e.g., in $NbSe_3$ where it is already seen around 145K[18]. However, no direct signature of FS nesting nor a CDW phase is observed in $TaSe_3$. Instead, the conduction electrons give rise to two branches of excitations, as traced by the maxima

of the EDCs in Figs. 2e and 2f. On the one hand there is a branch of "bare" excitations of a single electron, resulting in a parabolic conduction band with a fairly short life time showing up as a broad hump as a function of energy. On the other hand, the sharp quasiparticle excitations form a strongly renormalized and only weakly dispersive branch close the Fermi energy. They consist of conduction electrons that dress themselves with a cloud of bosonic excitons (most likely phonons) to form a heavy polaron band. The polaron band has a rich internal structure. The spectral weight is strongest close to k_F and becomes very weak for $k_y \approx 0$. Furthermore, the dispersion of the maximal spectral weight is not essentially flat as expected for a simple heavy polaron, but assumes the non-monotonic shape of a W (see Fig. 2g). Such a dispersion might arise due to the hybridization of the polaron band with a dispersing composite excitation consisting, e.g., of a conduction electron and a nearly soft phonon (which has not yet condensed). We will not explore these features in more detail here, but simply observe that they entail that the heavy polaron band effectively breaks up into two small islands concentrated just below the Fermi wave vectors $\pm k_F$. This will be important when we discuss exciton formation in the context of the SVBs.

Effects of surface doping. More insight into the SVBs is gained by increasing the density of surface electrons. This is achieved by evaporating potassium (K) in situ on the cleaved surface of $TaSe_3$. Figures 3a and 3b both show the ARPES intensity after evaporation for t1=1 minute, for the same range of momenta and energies as in Fig. 2b. The evaporation increases the chemical potential by about 230meV. The incoming photons are circular positive-helicity polarized in Fig. 3a and linearly horizontal polarized in Fig. 3b. EDCs as shown in Fig. 3c, allow to locate the MVB and the SVBs. The curvature intensity plot in Fig. 3d shows that the two SVBs (indicated by the red arrows) are more pronounced than in the undoped case of Fig. 2c. A heavy, but non-monotonically dispersing polaron band close to the Fermi energy is still present, but the size of the high intensity islands of diameter Δk within the polaron band increases together with k_F, as is apparent in Fig. 3d. (This would be expected if the W-shaped dispersion arose from hybridization with a replica band of the conduction band, displaced by the fixed momentum and energy of a fixed soft phonon.) The measured dispersions are traced in Fig. 3e. Note that the non-renormalized conduction band branch is essentially parabolic, apart from the polaronic effects close to the Fermi energy and the avoided level crossings with some SVBs, where the ARPES intensity is suppressed. For large enough momenta one identifies two SVBs roughly parallel to the MVB. At small momenta close to X, there are two nose-like dispersing pieces of an excitation branch. They might be continuations of the SVB's seen at larger momenta, as hinted in Fig. 3f. Figure 3g shows the ARPES intensity at $h\nu = 37$ eV after doping. Here, the first SVB is clearly visible. The doping strongly affects the average energy separations Δ_1 and Δ_2 between the MVB and the first SVB, and the first and second SVBs (if present), respectively. We measure these spacings in the regime of large momenta

relative to X. In Fig. 3h, Δ_1 and Δ_2 are seen to substantially increase with doping, i.e., with Fermi wave vector k_F. In particular, $\Delta_1 \sim$ 180 meV and $\Delta_2 \sim$ 70 meV, in the presence of potassium doping (t1) are much larger than the spacings $\Delta_1 \sim$ 70 meV and $\Delta_2 \sim$ 37 meV in undoped $TaSe_3$.

Interpretation of side bands. As is explained in the Supplementary Material and summarized in Fig. 4, the position, shape, and doping dependence of the SVBs can be best explained in terms of a moving bound state between the photo-hole in the valence band with nonzero group velocity and large momentum of a given chain and quasiparticles in the conduction bands on the same or on neighbouring chains Fig. 4a and b. In particular, for sufficiently large total momentum K along the chain (as compared to Δk, the diameter of the polaronic islands), we propose the following interpretation of the MVB and the SVBs. The MVB arises from the excitation of a single photo-hole in the valence band (Fig. 4c I). The top-most SVB above the MVB is the K-dependent threshold to a continuum consisting of an exciton and a free quasi-hole in the conduction band, the exciton being a moving bound state between a quasiparticle in the conduction band and a valence hole on the same chain, sharing the same group velocity (Fig. 4c II). The SVBs closer to the MVB can be of two distinct origins. One possibility is that the particle-hole excitation in the conduction band is created on a chain neighbouring that hosting the valence hole, leading to an inter-chain exciton (Fig. 4 c III), which has a lower binding energy than an intrachain exciton. Alternatively, one can have thresholds to more complex continua, the simplest consisting in a photo-hole accompanied by two particle-hole excitations on neighbouring chains (Fig. 4c IV), whereby both quasiparticles bind to the valence hole to form a mobile trion (also known as a charged exciton[22–24]). Such a threshold is expected to have a lower energy-integrated intensity, as it scales with a higher power of the density of conduction electrons (as it involves two particle-hole excitations), an aspect that might possibly rationalize the low intensity of the second SVB in Figs. 3c and d.

The separation of the SVBs from the MVB results from two sources. The binding energy of the exciton or trions is enhanced due to the effective one-dimensionality and the heavy mass of the polaronic quasiparticles, and it likely dominates over the energetic cost of the particle-hole excitation. This results in a (vertical) shift in energy of the SVB. Moreover, the valence hole does not take the full momentum K but transfers part of it to the conduction band. This entails a horizontal shift between MVB and SVB. The dominant momentum transfer is expected to be given by the diameter Δk of the high intensity islands in the polaron band. Since the latter increases with k_F, this rationalizes the increase of the separation between SVB and MVB with doping. Further details are discussed in the Supplementary Material.

Summary and outlook. The material $TaSe_3$ is a Q1D metal which combines a low density of conduction electrons with a polaronic renormalization of the low-energy quasiparticles. These ingredients all favour a non-negligible spectral weight in photoemission on composite excitations involving an exciton and a conduction band hole. Our experiments show that the excitons come in different favours depending on whether the involved holes and electrons belong to the same chain or not, or whether the hole binds one or two conduction electrons (resulting in an exciton or a trion, respectively). The thresholds to these composite bound state excitations are observed as side bands to the bare valence band, but at lower excitation energy. Indeed, if after electron emission the system is left with a bound state, it has absorbed strictly less energy than if only a single hole had been created, and it thus pushes the emitted photoelectron to higher energy above the MVB. Interchain excitons are Q1D cousins of bilayer excitons in layered 2D materials, such as transition metal dichalcogenides[25,26]. They are of particular interest as they may have a significantly longer life time than intra-chain excitons due to the spatial separation of the particle and the hole.

We have experimentally probed the evolution of these sidebands with increasing doping. The latter increases the typical momentum transfer in the conduction band, which increases the energy separation between the side and the main bands. At the same time screening increases which should lower the exciton binding energy, an effect that, however, appears to be subdominant in the range of explored doping. A more systematic study of this doping dependence will allow to follow the crossover from strong to weak interactions and to analyse the fate and nature of excitons as one crosses the Lifshitz transition where a second conduction band emerges at the Fermi level. It would also be interesting to excite the exciton bound states at low momenta by optical absorption, or by using stimuli, such as RIXS or even different from photons. Finally, it would be interesting to see whether dispersing excitons also exist in other trichalcogenides, at least in the regime of higher temperatures where they do not form a CDW. This will elucidate to what extent the peculiar structure of the polaronic band with its strong intensity islands is crucial for the visibility of exciton branches in ARPES.

Materials and Methods

Single crystals of $TaSe_3$ were synthesized using evenly-ground stoichiometric elemental Ta (~325 mesh, Beamtown Chemical, ≥ 99:9%) and Se (~ 200 mesh, Beamtown Chemical, ≥ 99:999%) with a total mass of ~300 mg were pressed into a pellet and placed in an evacuated quartz tube mixed with ~ 10 mg of I_2 as the vapor transport medium. The tube was put into a tube furnace and heated up to 700℃ on the sample side while the other side of the tube, while in the furnace, was open to the external environment so as to generate a temperature gradient. After holding the sample at 700℃ for five days, the furnace was shut down and cooled to room temperature. Needle-like crystals can be found at the cooler side of the quartz tube.

ARPES measurements were performed at the SIS-HRPES beam line with a Scienta R4000 analyser of the Swiss Light Source (PSI), and at the beamline UE112 PGM-2b-1^3 at BESSY (Berlin Electron Storage Ring Society for Synchrotron Radiation) Synchrotron. The energy and angular resolutions were set to 5 - 30meV and 0.1°, respectively. The samples for ARPES measurements were cleaved in situ and measured in a temperature range between 15K and 25K in a vacuum better than 8×10^{-11}Torr.

The first-principles calculations were performed within the framework of the full-potential linearized augmented plane-wave method implemented in the WIEN2K simulation package. A modified Becke-Johnson exchange potential together with the local-density approximation for the correlation potential was used to obtain accurate band structures. Spin-orbit coupling (SOC) was included as a second, self-consistent variational step. The radii of the muffin-tin sphere (R_{MT}) were 2.5 bohr for Ta and 2.38 bohr for Se. The k-point sampling grid of the BBZ in the self-consistent process was $7 \times 19 \times 6$. The truncation of the modulus of the reciprocal lattice vector K_{max}, which was used for the expansion of the wave functions in the interstitial region, was set to $R_{MT}K_{max} = 7$. The geometry optimization including SOC was carried out within the framework of the projector augmented-wave pseudopotential method implemented in the Vienna Ab initio Simulation Package. The ionic positions were relaxed until the force on each ion was less than 0.005 eV/Å.

Acknowledgments We acknowledge E. Rienks for help during the ARPES experiments. We thank Prof. Dirk van der Marel for discussions. This work was supported by the Sino-Swiss Science and Technology Cooperation (Grant No. IZLCZ2-170075), the Swiss National Science Foundation under Grant. No. 200021 166271, and the NCCR MARVEL funded by the Swiss National Science Foundation. This project has received funding from the European Union's Horizon 2020 research and innovation programme under the Marie Sklodowska-Curie grant agreement No. 701647. Funding by Deutsche Forschungsgemeinschaft through the Emmy Noether programme is gratefully

acknowledged (SE 2558/2-1). W.W.X. was supported by Beckman Young Investigator Program funded by Arnold and Mabel Beckman Foundation and US NSF-DMR-1944965. X. G. was supported by the US Department of Energy Division of Basic Energy Sciences (DG-FG02-98ER45706).

Author contributions: J.Z.M performed ARPES experiments with the help of M.N., J.J. and W.H.F; S.M.N. and Z.W performed first-principles calculations of the band structure. X.G and W.W.X. synthesised the single crystals. C.Y.X. performed primary high magnetic field quantum oscillation (QO) measurements with the help of J.Z.M., J.L.Z., T.S. and Y.M.X.; H.H. and U.D.G. analysed the possibility of boson driven band structures with the help of D.G. and O.Y.; I.K. performed Raman measurements for checking the phonon energy. N.K. and Y.S. performed primary transport measurements with PPMS. M.A.S. helped ruling out the bosonic strong coupling scenario; C.M. and M.M. analysed different physical scenario based on bound states and worked out the theory of excitonic side-bands. All authors contributed to the discussion of this project. J.Z.M., C.M., M.M. and M.S. wrote the manuscript. **Competing interests**: The authors declare that they have no competing interests. **Data and materials availability**: All data needed to evaluate the conclusions in the paper are present in the paper and/or the Supplementary Materials. Materials and additional data related to this paper may be requested from the authors.

References

1. Nagaosa, N. *Quantum Field Theory in Strongly Correlated Electronic Systems*. Theoretical and Mathematical Physics (Springer Berlin Heidelberg, 1999).

2. Giamarchi, T. & Press, O. U. *Quantum physics in one dimension*. International Series of Monogr (Clarendon Press, 2004).

3. Frenkel, J. On the transformation of light into heat in solids. *Phys. Rev.* **37**, 17–44 (1931).

4. Wannier, G. H. The structure of electronic excitation levels in insulating crystals. *Phys. Rev.* **52**, 191–197 (1937).

5. Kasha, M. Relation between Exciton Bands and Conduction Bands in Molecular Lamellar Systems. *Rev. Mod. Phys.* **31**, 162–169 (1959).

6. Knox, R. S. *Collective Excitations in Solids*. (*Springer US, Boston, MA, 1983*

1996). doi:10.1007/978-1-4612-4014-3_32.

7. Combescot, M. & Shiau, S. *Excitons and Cooper Pairs: Two Composite Bosons in Many-body Physics*. (Oxford University Press, 2016).

8. Wang, G. *et al.* Colloquium: Excitons in atomically thin transition metal dichalcogenides. *Rev. Mod. Phys.* **90**, 021001 (2018).

9. Hong, J., Senga, R., Pichler, T. & Suenaga, K. Probing Exciton Dispersions of Freestanding Monolayer WSe_2 by Momentum-Resolved Electron Energy-Loss Spectroscopy. *Phys. Rev. Lett.* **124**, 087401 (2020).

10. Seki, K. *et al.* Excitonic Bose-Einstein condensation in Ta_2NiSe_5 above room temperature. *Phys. Rev. B* **90**, 155116 (2014).

11. Sugawara, K. *et al.* Unconventional charge-density-wave transition in monolayer 1T-$TiSe_2$. *ACS Nano* **10**, 1341–1345 (2016).

12. Srivastava, S. K. & Avasthi, B. N. Preparation, structure and properties of transition metal trichalcogenides. *J. Mater. Sci.* **27**, 3693–3705 (1992).

13. Island, J. O. *et al.* Electronics and optoelectronics of quasi-1D layered transition metal trichalcogenides. *2D Mater.* **4**, 022003 (2017).

14. Sambongi, T. *et al.* Superconductivity in One-Dimensional $TaSe_3$. *J. Phys. Soc. Jpn.* **42**, 1421 (1977).

15. Tsutsumi, K. *et al.* Direct electron-diffraction evidence of charge-density-wave formation in $NbSe_3$. *Phys. Rev. Lett.* **39**, 1675–1676 (1977).

16. Yamamoto, M. Superconducting Properties of $TaSe_3$. *J. Phys. Soc. Jpn.* **45**, 431–438 (1978).

17. Haen, P., Lapierre, F., Monceau, P., Regueiro, M. & Richard, J. Low temperature

phase transition in the Chain-Like compounds $NbSe_3$ and $TaSe_3$. *Solid State Commun.* **26**, 725–730 (1978).

18. Ekino, T. & Akimitsu, J. Electron Tunneling Study of $NbSe_3$. *Jpn. J. Appl. Phys.* **26**, 625–626 (1987).

19. Cava, R. J., Fleming, R. M., Dunn, R. G. & Rietman, E. A. Low-frequency dielectric response of the charge-density wave in orthorhombic TaS_3. *Phys. Rev. B* **31**, 8325–8328 (1985).

20. Nagata, S., Kutsuzawa, H., Ebisu, S., Yamamura, H. & Taniguchi, S. Superconductivity in the quasi-one-dimensional conductor $TaSe_3$. *J. Phys. Chem. Solids* **50**, 703–707 (1989).

21. Nie, S. *et al.* Topological phases in the $TaSe_3$ compound. *Phys. Rev. B* **98**, 125143 (2018).

22. Lampert, M. A. Mobile and immobile effective-mass-particle complexes in nonmetallic solids. *Phys. Rev. Lett.* **1**, 450–453 (1958).

23. Kheng, K. *et al.* Observation of negatively charged excitons X- in semiconductor quantum wells. *Phys. Rev. Lett.* **71**, 1752–1755 (1993).

24. Matsunaga, R., Matsuda, K. & Kanemitsu, Y. Observation of charged excitons in hole-doped carbon nanotubes using photoluminescence and absorption spectroscopy. *Phys. Rev. Lett.* **106**, 037404 (2011).

25. Rivera, P. *et al.* Observation of long-lived interlayer excitons in monolayer $MoSe_2$-WSe_2 heterostructures. *Nat. Commun.* **6**, 6242 (2015).

26. Unuchek, D. *et al.* Room-temperature electrical control of exciton flux in a van der Waals heterostructure. *Nature* **560**, 340–344 (2018).

27. Langreth, D. C. Singularities in the x-ray spectra of metals. *Phys. Rev. B* **1**, 471–477 (1970).

28. Mahan, G. D. *Many-Particle Physics*. (Kluwer Academic/Plenum Publishers, 2000). doi:10.1007/978-1-4757-5714-9.

29. Caruso, F., Verdi, C. & Giustino, F. *Many-Body Calculations of Plasmon and Phonon Satellites in Angle-Resolved Photoelectron Spectra Using the Cumulant Expansion Approach*. (Springer, Cham, 2018). doi:10.1007/978-3-319-42913-7_2-1.

30. Lee, J. J. *et al.* Interfacial mode coupling as the origin of the enhancement of Tc in FeSe films on $SrTiO_3$. *Nature* **515**, 245–248 (2014).

31. Wang, Z. *et al.* Tailoring the nature and strength of electron-phonon interactions in the $SrTiO_3$ (001) 2D electron liquid. *Nat. Mater.* **15**, 835–839 (2016).

32. Riley, J. M. *et al.* Crossover from lattice to plasmonic polarons of a spin-polarised electron gas in ferromagnetic EuO. *Nat. Commun.* **9**, 2305 (2018).

33. Chen, C. *et al.* Emergence of Interfacial Polarons from Electron-Phonon Coupling in Graphene/h-BN van der Waals Heterostructures. *Nano Lett.* **18**, 1082–1087 (2018).

34. Chen, C. *et al.* Robustness of topological order and formation of quantum well states in topological insulators exposed to ambient environment. *Proc. Natl. Acad. Sci. U. S. A.* **109**, 3694–3698 (2012).

35. Wang, Z. *et al.* Atomically Precise Lateral Modulation of a Two-Dimensional Electron Liquid in Anatase TiO_2 Thin Films. *Nano Lett.* **17**, 2561–2567 (2017).

36. Mahan, G. Excitons in Metals: Infinite Hole Mass. *Phys. Rev.* **163**, 612–617

(1967).

37. Mahan, G. D. Excitons in Degenerate Semiconductors. *Phys. Rev.* **153**, 882–889 (1967).

38. McGuire, J. B. Interacting fermions in one dimension. I. Repulsive potential. *J. Math. Phys.* **6**, 432–439 (1965).

39. McGuire, J. B. Interacting fermions in one dimension. II. Attractive potential. *J. Math. Phys.* **7**, 123–132 (1966).

40. Combescot, M. & Nozières, P. Infrared catastrophy and excitons in the X-ray spectra of metals. *J. Phys.* **32**, 913–929 (1971).

41. Edwards, D. M. Magnetism in Single-Band Models: Exact One-Dimensional Wave Functions Generalised to Higher Dimensions. *Prog. Theor. Phys. Suppl.* **101**, 453–461 (1990).

42. Castella, H. & Zotos, X. Exact calculation of spectral properties of a particle interacting with a one-dimensional fermionic system. *Phys. Rev. B* **47**, 16186–16193 (1993).

43. Eßler, F. H. L. & Frahm, H. X-ray edge singularity in integrable lattice models of correlated electrons. *Phys. Rev. B* **56**, 6631–6641 (1997).

44. Affleck, I. Boundary condition changing operators in conformal field theory and condensed matter physics. *Nucl. Phys. B* **58**, 35–41 (1997).

45. Zagoskin, A. M. & Affleck, I. Fermi edge singularities: Bound states and finite-size effects. *J. Phys. A. Math. Gen.* **30**, 5743–5765 (1997).

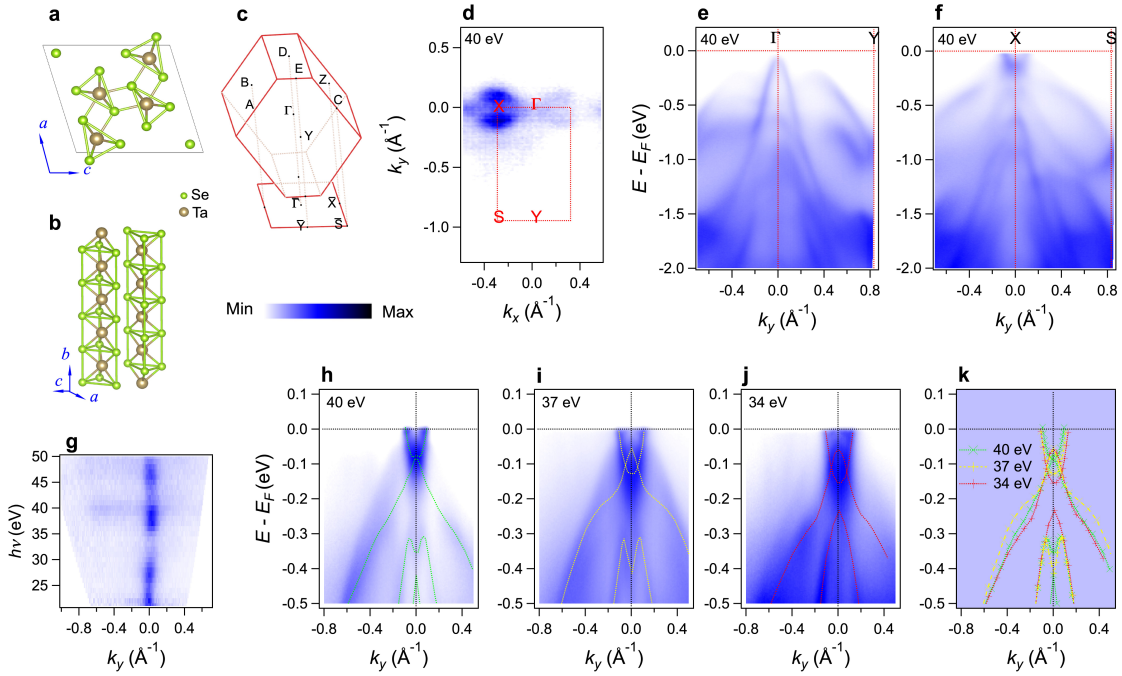

FIG. 1. The crystalline and electronic structures of $TaSe_3$ at 19K. The crystallographic axis are *a*, *b*, and *c*. **a**, Crystal structure projected onto the *a*-*c* plane. **b**, Crystal structure with its 1D chains oriented along the b axis. **c**, The bulk Brillouin zone BBZ and the 2D surface Brillouin zone SBZ of the cleavage surface [normal to $(10\bar{1})$]. **d**, ARPES intensity at the Fermi energy E_F as a function of the momentum $k \in$ SBZ for incoming photon energy $h\nu$= 40 eV. The momenta k_x and k_y are conjugate to the (101) and the (010) direction, respectively. **e** and **f**, ARPES intensities at $h\nu$ = 40eV as a function of the energy E - E_F and the momentum component k_y in the SBZ, along the cut Γ-Y (k_x = 0) in e, and along the cut X-S in f. **g**, ARPES intensity as a function of the momentum k_y and of the incoming photon energy $h\nu$, which tunes the momentum $k_\perp$ perpendicular to the planes. The cross-section of the Fermi surface is seen to be very elongated along $k_\perp$, suggesting that the Fermi surface is essentially an elliptical cylinder with axis parallel to $k_\perp$. **h-j**, ARPES intensities as a function of the energy E - E_F and the momentum k_y along the cut X-S in the SBZ for photon energies $h\nu$ = 40 eV in h, $h\nu$ = 37 eV in i, and $h\nu$ = 34 eV in j. **k**, Superimposed band dispersions from panels h-j (shown as coloured continuous lines as guide to the eye). The variation with $h\nu$ implies a finite dispersion along $k_\perp$.

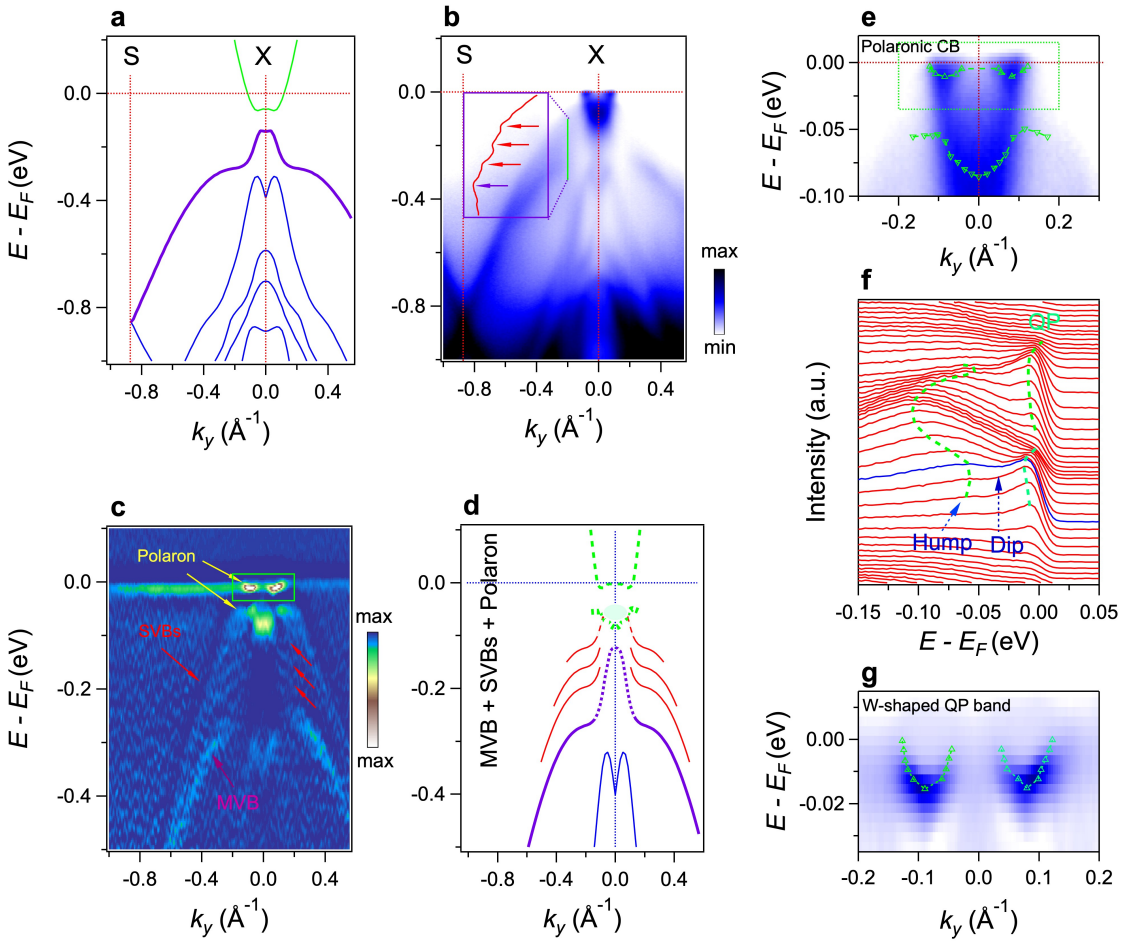

FIG. 2. Polaron conduction band and side valence bands. **a**, Dispersion of the noninteracting (Bloch) bands of $TaSe_3$ computed using DFT (see method part). The purple band is the topmost valence band, which we refer to as the MVB. It lies between one conduction band (coloured in green) and four lower lying valence bands (coloured in blue). The dispersion of all bands is symmetric about X along the X-S cut for constant $k_\perp = 0$. **b**, ARPES data from Fig. 1f with higher energy resolution and statistics. The curve in the inset shows the EDC along the green line ($k_y = -0.2 Å^{-1}$). The horizontal axis in the purple box shows the spectra intensity. The red arrows point to side peaks. Their dispersions with momentum define "side valence bands" (SVBs). **c**, The curvature intensity plot corresponding to the data in b enhances the visibility of SVBs marked by red arrows above the MVB. The green box encloses the coherent branch of the polaron quasiparticles (QPs) making up the bottom of the conduction band and whose spectral weight is concentrated in two small islands of diameter Δk. The broad hump indicated by a yellow arrow is the remnant of the CB that would be left, were there no interaction with a bosonic mode. **d**, Schematical interpretation of the signatures seen in c. **e** and **f**, Close up of the data of b. The upper and lower dashed lines in e trace the dispersions of the polaron QP peak and the broad hump through peaks from EDCs, respectively, as visible in the equally offset EDCs at different momentum in f. **g**, Detailed view of the ARPES intensity within the polaron band in the green box of c. The dashed green line indicates the extrapolated dispersion of the W-shaped QP band.

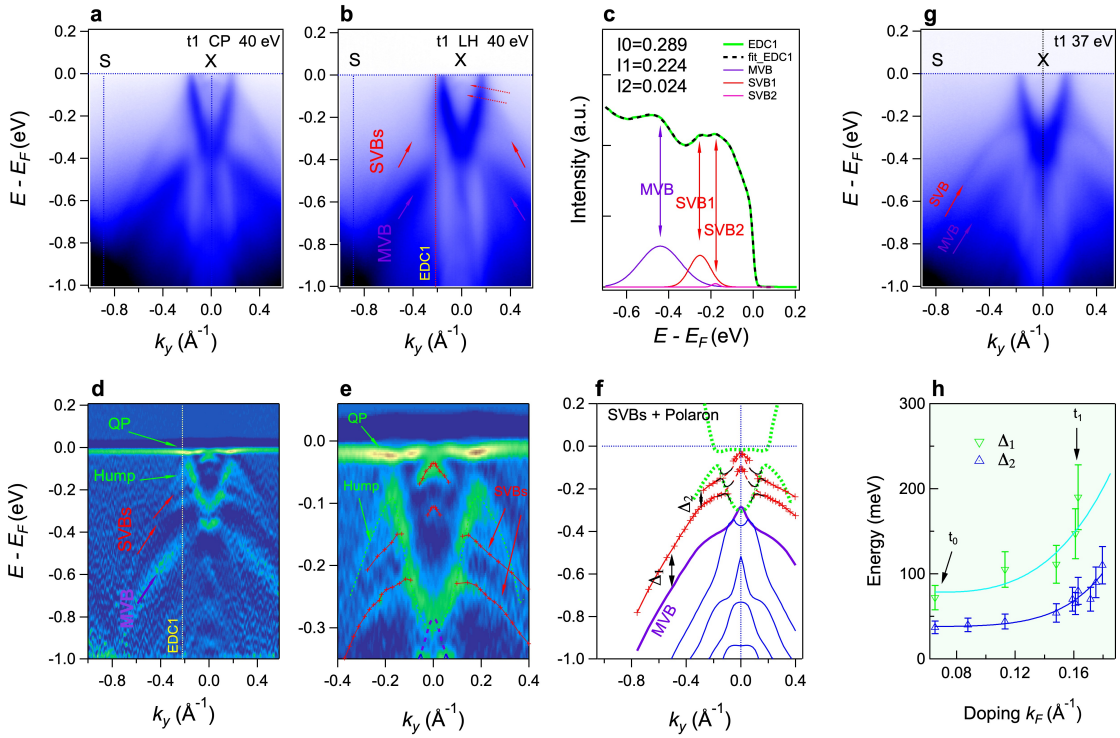

FIG. 3. Dependence on potassium doping of the electronic structure of $TaSe_3$ at 19K. **a** and **b**, ARPES intensity plot with energy measured relative to E_F and momenta along the X-S cut, after potassium was deposited for t1=1 minute on the surface of $TaSe_3$. The incoming photons are circular positive-helicity [CP, a] and linearly horizontal [LH, b] polarized, respectively. The full red arrows in b indicate a side valence band (SVB) above the main valence band (MVB), to which the purple arrow points. The dashed red arrows indicate additional spectral side-features at small k_y, also seen in a. **c**, The energy distribution along the line EDC1 in b. Two side peaks, a strong one (SVB1) and weak one (SVB2), are visible at $k_y = -0.2\ \dot{A}^{-1}$. **d**, The curvature intensity plot of the ARPES intensity in b. The two SVBs are indicated by red arrows. The MVB peak is indicated by a purple arrow. The coherent polaron peak (QP) and the bare CB excitation (hump) are indicated by green arrows. **e**, The close up of the curvature intensity plot in d identifies the sidebands more clearly. The red lines show the two SVB dispersions extracted from the peak positions in the curvature intensity plot. Additionally, we delineate nose-like side spectral features at small k_y. **f**, The band dispersions extracted from tracing the peak positions of the full spectrum in d. The green dotted lines are the polaronic conduction band and the dispersing hump of the bare CB excitation. The red lines at small $k_y \approx 0$ are sidepeaks whose vertical shift relative to the SVBs at large momenta is similar to that of the "nose"-like peak predicted by the DFT calculations of Fig. 2a with respect to the MVB dispersion at large k_y. The dotted red lines suggest that these side-features might be of similar origin and form a band, which is however interrupted by avoided crossings (indicated by thin black lines) with the bare CB (hump). **g**, ARPES intensity as a function of energy relative to E_F and momentum k_y along the X-S cut recorded with $h\nu = 37$ eV, after potassium was deposited for 1 minute on the surface of $TaSe_3$. **h**, The average energy separations Δ_1 (between MVB and the first SVB) and Δ_2 (between the first and the second SVB), (see panel f), plotted as a function of the measured Fermi wave vector k_F, which is tuned by the evaporation time of potassium.

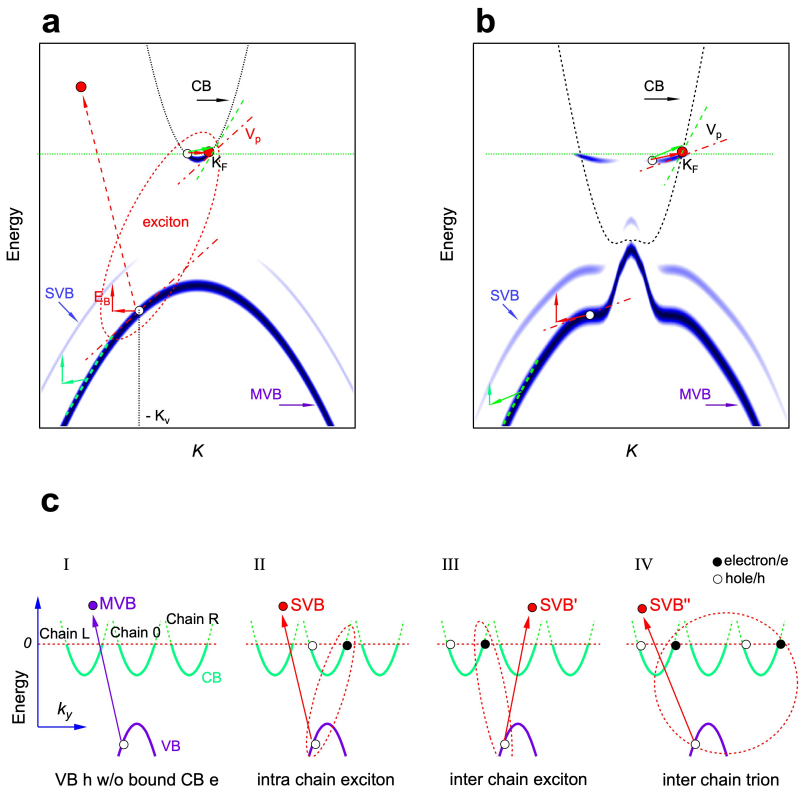

FIG. 4. Excitonic sidebands are due to composite excitations that simultaneously create a VB hole and a p-h excitation in the CB, whereby the VB hole and the conduction electron have the same group velocity and thus can form a mobile bound state. **a**, Toy model with parabolic VB and CB. The drawing shows excitonic excitations for total momenta $K > K^*$ where a VB hole with velocity $v_h > v_F$ binds to a CB electron above the Fermi level. The side band is constructed graphically. Starting from a VB state, the partner state with equal group velocity (slope of the dispersion) in the CB is determined. The energy- momentum transfer from the left Fermi point to that state is combined with a vertical shift by the (momentum independent) binding energy to obtain a point on the excitonic side branch. **b**, The same procedure applied to a more realistic model of $TaSe_3$. The simple parabolic Fermi sea is replaced by high intensity islands in the polaronic band, its diameter Δk playing the role of $2k_F$ in a. The binding energy now depends on the curvature of the VB and the CB at the momenta involved in the exciton pair. The side band construction results in an excitonic branch which is a nearly parallel translate of the simple hole dispersion, the MVB. **c**, Proposed origin of the MVB and the various SVBs. The MVB (I) results from a single VB hole excitation. It costs less energy (at given momentum K) if it is accompanied by particle-hole excitations in the CB of the same or neighbouring chains. The binding of the CB particle(s) with the VB hole results in various types of excitonic modes, namely intra-chain exciton (II), inter-chain excitons (III), and possibly inter-chain trions (IV).

Supplementary materials for

Multiple mobile excitons manifested as sidebands in metallic phase of $TaSe_3$

J.-Z. Ma, S.-M. Nie, X. Gui, M. Naamneh, J. Jandke, C. Y. Xi, J. L. Zhang, T. Shang, Y.M. Xiong, I. Kapon, N. Kumar, Y. Soh, D. Gosalbezmartinez, O. Yazyev, W.H. Fan, N. Plumb, M. Radovic, H. Hubener, U. D. Giovannini, M. Sentef, W.-W. Song, Z. Wang, C. Mudry, M. Muller, M. Shi.

**Corresponding to: junzhang.ma@psi.ch, markus.Mueller@psi.ch, ming.shi@psi.ch*

This file contains

1, main text of the supplementary materials.

2, Figures S1, and S2.

The replica of the MVB have several characteristics that rule out standard scenario that are known to yield side bands. The coupling between the electrons and a collective bosonic excitation of a well-defined frequency can generate equally spaced shake-off bands[27–29], as observed in ARPES spectra of materials like TiO_2, EuO, graphene on hexagonal boron nitride, and monolayer of FeSe on $SrTiO_3$[30–33]. However, those occur all *below* the MVB for weak coupling (see Fig. S1a), or at best in roughly equal numbers above and below the MVB for strong coupling but not experimentally reported yet by photoemission (see Fig. S1b), with *equidistant energy separations* in either case[27]. In addition to this discrepancy with our data for $TaSe_3$ it would be difficult to identify a specific bosonic mode whose frequency would fit the average energy separation Δ_1 (which is far below typical plasmon energies and above the highest phonon mode energy) and would strongly depend on doping. A second frequent cause for observing multiple copies of a band are finite-size artifacts such as when few surface layers are either nearly disconnected from the bulk and thus effectively form a 2D thin film or are subject to a confining surface potential as happens for the surfaces of 3D topological insulators[34] or 3D semiconductors[35] and are known from edge-reconstruction effects in 2D electron gases. In either case the confinement perpendicular to the surface could cause multiple sidebands. This is, however, ruled out because (i) all bands would appear with multiple copies, and (ii) the spacing of the sidebands would be dictated by the layer thickness rather than by the doping. Moreover,

explicit calculations predict much smaller spacings than the observed values as shown in Fig. S2.

The coupling to a bosonic oscillator invariably generates side bands below the MVB, because the oscillator can always be left in a higher excited state. The absence of sidebands below the MVB thus suggests that we are dealing with a coupling to fermionic degrees of freedom, for which the spectrum due to a specific fermionic mode is bounded by Pauli blocking. Side peaks that only appear above a main peak are indeed known to occur in valence hole emission processes in the presence of a small Fermi sea in the conduction band[36,37]. A necessary prerequisite is that the valence hole binds with an excited electron from the unoccupied conduction band[38–45]. Such effects are strongest in low effective dimensionalities. A large body of literature has considered the limit of immobile holes (a flat valence band)[36,37,40], due to its exact solvability. Here, we present a qualitative description for the general case of valence holes of finite mass.

We start from a 1D toy model consisting of a filled parabolic valence band (VB) of mass $-m_h < 0$ and a conduction band (CB) of mass $m_e > 0$, filled up to the Fermi momentum $k_F \equiv m_e v_F > 0$, with a density $n_c \equiv k_F/\pi$ of conduction electrons. We assume a contact attraction of the form $-g\delta(y_h - y_e)$ with $g > 0$ between a photo-induced hole in the VB and any electron in the CB, having positions y_h and y_e, respectively. We focus on excitations involving a valence hole of momentum k_h, having the group velocity $|v_h| = |k_h|/|m_h| > v_F$. The hole emission process for which we expect the largest matrix element corresponds to the creation of a hole with the momentum

$$K \coloneqq k_h \tag{A1a}$$

and the energy

$$E_{MVB}(K) \coloneqq \frac{K^2}{2m_h} - E_{MF} \tag{A1b}$$

where $E_{MF} \equiv gn_c = gk_F/\pi$ is the mean-field interaction between the hole and the conduction electrons. At the same total momentum K there are, however, more complex excitations where a hole in the VB with the momentum k_h occurs simultaneously with a particle-hole pair in the CB. The latter promotes an electron from an occupied state in the Fermi sea with momentum $k'_e \in [-k_F, k_F]$ to an unoccupied state above the Fermi sea with momentum $|k_e| > k_F$, involving a momentum transfer $q \equiv k_e - k'_e$.
Such an excitation carries the total momentum

$$K \coloneqq k_h + q = k_h + k_e - k'_e \tag{A2a}$$

and the energy

$$E_3(k_h, k_e, k'_e) \coloneqq \frac{k_h^2}{2m_h} + \frac{k_e^2 - k_e'^2}{2m_e} - E_{MF} \tag{A2b}$$

Minimizing this three-particle energy at fixed total momentum K, one finds the following. Let $v_h = k_h/m_h$ be the velocity of the hole (we may assume $v_h > 0$ without loss of generality). If $v_h > v_F$, the minimum occurs when the particle in the CB moves at the same velocity as the VB hole, $k_e/m_e = v_e = v_h$, while $k'_e = -k_F$ sits at the Fermi level. For $v_h < v_F$ instead, the minimum occurs when the hole in the Fermi sea moves at opposite velocity to that of the VB hole, $\frac{k'_e}{m_e} = v'_e = -v_h$, while $k_e = +k_F$ sits at the Fermi level. In either case the total momentum is $K = v_h(m_e + m_h) + k_F$. The dispersion of the three-particle threshold energy in the weakly interacting limit is

$$E_{3,min}(K) \coloneqq \tfrac{1}{2} m_h v_K^2 + \tfrac{1}{2} m_e |v_K^2 - v_F^2| - E_{MF} \tag{A3a}$$

where

$$v_K \coloneqq (K - k_F)/(m_h + m_e) \tag{A3b}$$

is the velocity of the valence band hole in the three particle state with momentum K and minimal energy. This threshold energy lies strictly below the energy (A1b) of a single hole excitation. Note the kink in the dispersion at

$$K = K^*, \;\; K^* \coloneqq 2k_F + m_h v_F \tag{A3c}$$

where v_k crosses v_F.

The above expression does not take into account, however, the possibility that the VB hole and the CB electron might interact so strongly with each other that they form a bound state. Indeed, this happens when $v_h = v_e$ (within an uncertainty of order g). This exciton condition is precisely fulfilled at the 3-particle threshold, for any $K > K^*$. The exact solution for the two-body problem of a VB hole interacting with a CB electron confirms the existence of a dispersing exciton bound state under this condition with the dispersion

$$E_{exciton}(K) = E_{3,min}(K) - E_B, \quad E_B = \frac{g^2}{2} \frac{m_h m_e}{m_h + m_e} \tag{A4}$$

As the nonvanishing positive binding energy E_B is subtracted from the dispersion (A3a), the exciton branch (A4) is pulled below the three-particle continuum (A2b). Note that the binding energy E_B is the larger the heavier the involved particles are, and the larger the attraction g is. A graphic construction of the dispersion (A4) is shown in Fig. 4a.

For $K < K^* - O(g)$, there are still excitonic states (having minimal energy for $v_h = v_e = v_F$), but their total energy lies inside the three-particle continuum. An exact solution for the case of equal masses, $m_h = m_e$ is available for the full many-body problem of a hole in the presence of the Fermi sea in the CB[39]. It confirms the above dispersion at large momenta to great accuracy, with only parametrically small corrections to the interaction energy E_{MF} for $K \gg K_F$.

The energy difference between the simple hole branch (A1) and the exciton branch for $K > K^*$ is strictly positive,

$$E_{MVB}(K) - E_{exciton}(K) = \frac{m_e}{m_h}\frac{(K+m_h v_F)^2}{2(m_e+m_h)} + E_B \quad \text{(A5)}$$

and, at fixed K, increases with k_F.

We now seek to translate the key insights drawn from our toy model (a 1D Hamiltonian with two parabolic bands and a contact interaction between a single VB hole and N_F electrons from the CB) to the measured ARPES spectra of $TaSe_3$, which has much more complex dispersive bands. To this end, we consider a plane of the material $TaSe_3$ as consisting of parallel and weakly coupled chains. For simplicity, we treat each chain as a 1D conductor with a low density n_F of electrons in its CB. We also neglect the hopping between the chains. The presence of weakly coupled chains allows for the possibility of excitons that bind a MVB hole with an excited CB electron on different chains, if the difference between the respective binding energies exceeds the hopping between the chains. Since the binding energies seem to be substantial in the present material, we believe that such interchain excitons can explain the observed multiplicity of sidebands. Further possibilities will be discussed below.

In contrast to our toy model, the CB does not disperse like a simple parabola. Rather, close to the Fermi energy, the quasiparticles of the CB are heavy, renormalized polarons, whose spectral weight is concentrated in two small islands close to $\pm k_F$, whose diameters Δk increase with increasing k_F. For the purpose of excitons, these islands act like two small and shallow Fermi seas with heavy particles of mass m_e. An excitation with total right-moving momentum K exceeding Δk can be composed of a MVB hole of momentum $\approx K - \Delta k$ and a particle-hole excitation from the left-moving edge of such an island to just above the right-moving Fermi point, whereby the group velocity of the particle excitation must match that of the MVB hole. The binding energy E_B of the exciton that forms is the highest for MVB holes in a regime of momenta with a high effective mass (i.e., with a small curvature in the dispersion). This is the case at intermediate momenta where the MVB displays relatively flat shoulders in its dispersion. At smaller momenta around the "knee" where the curvature of the MVB changes sign, excitons cannot form except under strong coupling. At yet smaller momenta where the MVB predicted by DFT has a much steeper slope, the effective mass, and thus the binding energy E_B, is small. In this region, even the continuation of the MVB is hardly visible in the ARPES data. The sideband may be even harder to detect since the group velocity of the MVB hole and the involved CB electron is large, the corresponding density of states is low, and the matrix element for the excitation decreases. Close to the top of the MVB, around $k_y = 0$, for which MVB group velocities are not far from v_F, it is possible that a bound state forms involving particle-hole excitations with very small momentum transfer $q < \Delta k$. Those may result in side peaks to the main hole excitation branch as well. Composite excitations of this type might be at the origin of the nose-like spectral features close to $k_y = 0$ especially in Fig. 3, where we suggest

how they might connect to the sidebands at larger momenta while undergoing some avoided crossings with the bare CB parabola.

In the toy model with quadratic dispersions, the separation between the VB (the single hole excitation) and the side bands (the exciton band) increases with $2k_F$, i.e., the momentum transfer across the Fermi sea. In the case of $TaSe_3$, however, the relevant momentum transfer is the diameter Δk of the polaron islands, which is empirically found to increase with doping and thus with k_F. Beyond the Fermi points, the CB starts dispersing rather rapidly. If so, the momentum transfer required to match the velocity of a MVB hole does not exceed Δk by much. A graphic construction of the SVB due to exciton formation for $TaSe_3$ is shown in Fig. 4b. A given MVB hole with the pair $(k_h, \varepsilon_h(k_h))$ of quantum numbers gives rise to an excitonic side peak, which is displaced by the momentum and energy transfer $(k_e - k'_e \approx \Delta k, \varepsilon(k_e) - \varepsilon(k'_e))$ of the particle-hole excitation. The side peak is additionally displaced in energy by the binding energy E_B, which is larger in the flatter portions of the VB. This results in a SVB which is a nearly parallel translation of the MVB. The separation of SVBs from the MVB (as measured above the flat shoulder) is composed of the binding energy E_B and a contribution from the momentum transfer Δk to the CB. The latter translates into a vertical separation $v_h \Delta k$, where v_h is a typical group velocity in the latter shoulder of the MVB. As shown in Fig. 3j, this separation indeed increases with doping, or equivalently, with k_F and thus Δk.

Doping increases not only the energy separations between MVB and SVBs, but it also enhances the intensity of the SVBs (integrated over energy at fixed momentum). This is to be expected qualitatively as the phase space for particle-hole excitations resulting in excitons increases essentially linearly with the density n_c in the conduction band. Since we assume that a MVB hole on a given chain may come along with a particle-hole excitation on a neighbouring chain, it may as well be possible to create composite excitations involving two particle-hole excitations (e.g., on two different neighbouring chains), with the two CB electrons binding to the VB hole to form a trion. Such a side band would come with a smaller phase space, scaling as n_c^2. The fit of the side peak intensities in Fig. 3c suggests that the second side peak has significantly weaker intensity than the first side peak (the third side peak being buried by the hump feature of the CB). This might hint that the second SVB could be associated with such a trionic excitation. This would also be in line with the observation that the separation Δ_2 from the first side band increases with k_F, which is not expected if all side bands are excitonic excitations involving a momentum transfer of the same order Δk.

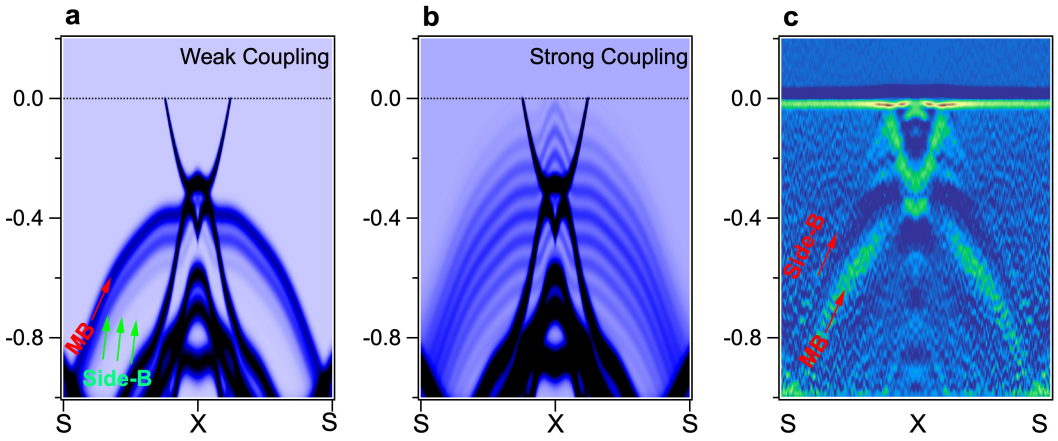

Fig. S1. Comparison between the band structure of $TaSe_3$ when coupled to a single bosonic oscillator and ARPES intensities on $TaSe_3$. **a** and **b**, The calculated band structure along the S-X cut for weak and strong coupling to the single bosonic mode, respectively. **c**, ARPES curvature intensity along the S-X cut, after symmetrisation of the data about X.

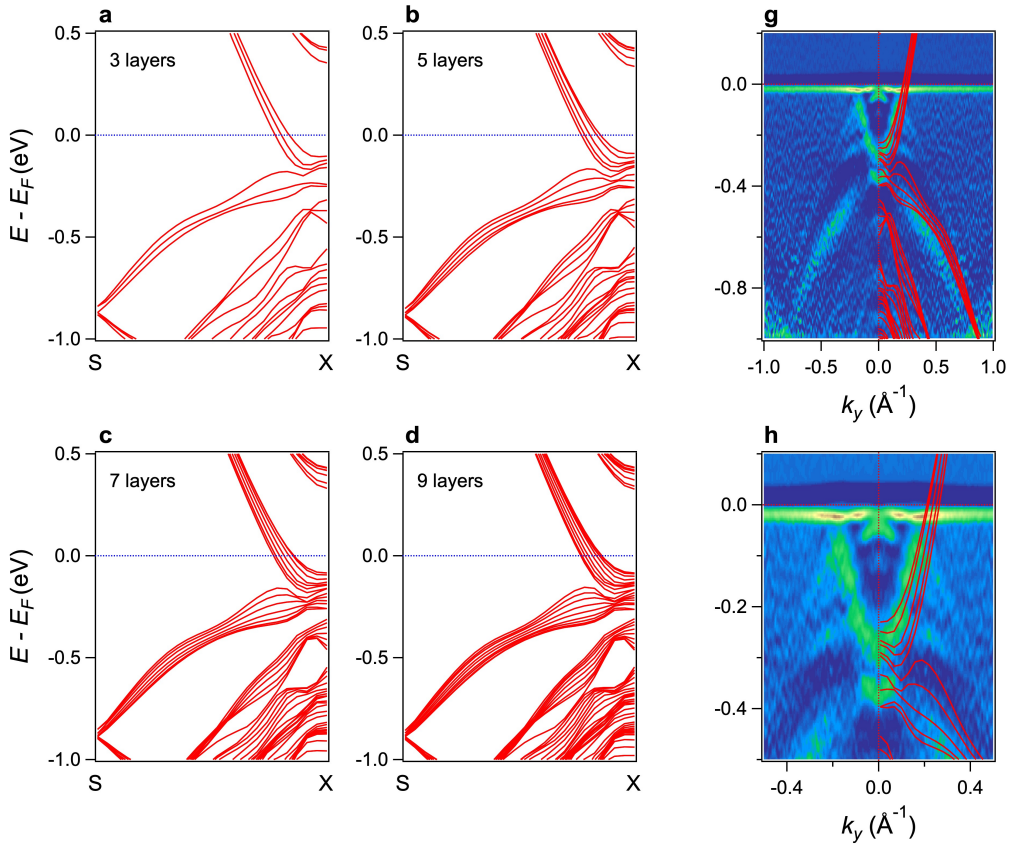

FIG. S2. Comparison between the band structure of $TaSe_3$ modelled in a slab geometry with ARPES intensities. **a-d**, The calculated band structure along the S-X cut in the SBZ when the slab contains 3, 5, 7 or 9 unit cells along the $(10\bar{1})$ direction. **g** and **h**, ARPES curvature intensity along the S-X cut after symmetrisation of the data about X, superposed with the bands of panel b.